

Counting photons at low temperature with a streaming time-to-digital converter

P. C. F. Di Stefano^a, P. Nadeau^a, C. J. G. Onderwater^b, C. Trudeau^a,
M.-A. Verdier^a

^a*Department of Physics, Engineering Physics & Astronomy, Queen's University, Kingston,
ON, Canada, K7L 3N6*

^b*Kernfysisch Versneller Instituut, University of Groningen, NL-9747AA Groningen, The
Netherlands*

Abstract

We present some aspects of photon counting to study scintillators at low temperatures. A time-to-digital converter (TDC) had been configured to acquire several-minute-long streams of data, simplifying the multiple photon counting coincidence technique. Results in terms of light yield and time structure of a ZnWO₄ scintillator are comparable to those obtained with a fast digitizer. Streaming data also provides flexibility in analyzing the data, in terms of coincidence window between the channels, and acquisition window of individual channels. We discuss the effect of changing these parameters, and use them to confirm low-energy features in the spectra of the number of detected photons, such as the 60 keV line from ²⁴¹Am in the ZnWO₄ sample. We lastly use the TDC to study the transmission of the optical cryostat employed in these studies at various temperatures.

Keywords: rare event search, scintillation, low temperature, photon counting, decay time, light yield

1. Introduction

1
2 Rare-event searches such as those for neutrinoless double beta decay or for
3 dark matter have fueled recent interest in developing cryogenic scintillators for
4 particle detection [1, 2]. For a given energy deposited by a particle in a scintil-
5 lator, the amount of light emitted depends on the nature of the particle. When
6 coupled to the measurement of phonons that is possible at low temperature (gen-
7 erally below 100 mK) and that provides the deposited energy, the measurement
8 of scintillation photons therefore allows particle identification, and rejection of a
9 significant fraction of the radioactive background in rare-event searches [3]. The
10 wealth of known room-temperature scintillators [4] also motivates the study of
11 scintillators at low-temperature.

Email address: distefan@queensu.ca (P. C. F. Di Stefano)

12 A typical method to study scintillators at low temperatures involves an opti-
13 cal cryostat with photomultipliers (PMs) at room temperature. When a particle
14 interacts in the cooled scintillator sample, the latter emits light that can escape
15 the cryostat and be detected by the PMs [5]. One useful method is the multiple
16 photon counting coincidence (MPCC) technique [6]. Its hardware component
17 uses the scintillation-induced coincidence between two PMs observing the crys-
18 tal to start digitizing the signals of each PM. Requiring a coincidence between
19 the PMs can greatly reduce the number of recorded background events (from
20 dark currents, for instance), though spurious coincidences from backgrounds
21 can remain. Offline, software extracts the arrival time and other information
22 for each photon found in the trace. The light yield is then determined from the
23 number of photons, and the pulse shape is determined from the photon arrival
24 times. Compared to other methods like the delayed-coincidence technique [7],
25 the MPCC technique is well suited to the long time constants occurring at low
26 temperatures, often greater than $100 \mu\text{s}$, and supplies information on the num-
27 ber of photons emitted (and thus the light yield of the scintillator) in addition to
28 just timing information. However, the quantity of acquired data is voluminous,
29 as is the time required to process it. Moreover, the result of the procedure (a
30 list of photon times) is similar to what one would obtain from a single-start-
31 multi-stop time-to-digital converter (TDC); this motivates the use of an actual
32 TDC instead. Indeed, multi-stop TDCs have already been used to increase the
33 acquisition rate of the delayed-coincidence technique [8]. In addition, a TDC
34 may be able to write long streams of photon arrival times for each PM, thereby
35 allowing flexibility in choosing the coincidence and acquisition windows offline,
36 rather than having to set them ahead of time as is the case with the standard
37 setup.

38 In this paper, we present the TDC we have used for this variant of the MPCC
39 method, and compare its results to the standard, digitizer based, method. We
40 discuss optimization of the coincidence and acquisition parameters, and their
41 influence on the low energy spectrum obtained with a ZnWO_4 crystal and ^{241}Am
42 radioactive source. Lastly, we use the TDC to also characterize the transmission
43 of our optical cryostat

44 2. Running the TDC in streaming mode

45 The standard MPCC method [6] allows simultaneous measurement of light
46 yield and time structure of scintillators. It is well adapted to the long time
47 constants (of the order of $100 \mu\text{s}$ or greater) that can be encountered at low
48 temperatures, and relies on a hardware component and a software one. It
49 requires a hardware trigger (for instance the coincidence between two photo-
50 multipliers, that can be as long as $1 \mu\text{s}$ or greater) to start a digitizer (i.e.
51 analog to digital converter or ADC) reading one or more photomultiplier tubes
52 for a fixed duration. A whole pulse trace is digitized each time, with a short
53 enough sampling (typically between 1 ns and 20 ns depending on the PMs and
54 preamplifiers) to resolve individual photoelectrons. Offline, software identifies
55 individual photons in each pulse, and extracts mainly the arrival time of each

56 photon. Software cuts are then applied to remove spurious events from the set,
57 and build spectra and pulse shapes. The hardware and photon identification
58 algorithms function in essence like a single-start-multi-stop time-to-digital con-
59 verter (TDC); however, the quantity of data generated by the digitizer may be
60 quite large (10000 events digitized on two channels with a sampling of 1 ns for
61 a duration of 1 ms at a resolution of 8 bits amounts to 20 Gbytes of data¹), and
62 the time required to process it also, hence the motivation to use an actual TDC
63 that would read the photomultiplier tubes directly. One possibility would be
64 to use a hardware coincidence between two photomultipliers to start the TDC.
65 However, since most TDCs do not possess a pretrigger memory, this would lead
66 to the loss of all early photons before the second photon which determines the
67 coincidence. In addition, it is not practical to delay the TDC signal by the
68 duration of the coincidence window (often greater than 1 μ s) or more because
69 of signal attenuation.

70 We have therefore turned our attention to running a TDC in continuous,
71 streaming, mode. In this configuration, the TDC is started at an arbitrary
72 time, and then acquires stop signals (hereafter simply referred to as stops) nearly
73 continuously during a run, i.e. a duration of the order of an hour broken into
74 segments of several minutes. Though TDCs able to run in this mode exist off-
75 the-shelf (e.g. FAST ComTec GmbH MCS6A), we have access to a Compact PCI
76 Agilent U1051A (TC890) that requires a slightly modified configuration [9, 10].
77 In standard operation, following a start signal on a dedicated channel, stop
78 signals on up to six channels are recorded up to the next start signal or for
79 10.48 ms at most. Nominal retriggering time of each channel is 15 ns, and
80 nominal time resolution on individual triggers of 0.05 ns. The device in fact has
81 two memory banks that can operate alternately, allowing continuous acquisition
82 of stops over longer periods of time, for instance by using a repetitive start
83 function with a period smaller than 10.48 ms — provided the rate of events
84 is reasonable. To obtain a continuous stream, we triggered the TDC with a
85 National Instruments PXI 5422 function generator running at 110 Hz, in view
86 of concatenating the resulting segments into a nearly continuous stream, as
87 illustrated in Figure 1. The TDC records stop times relative to the nearest
88 start, so reconstructing a stream of stops much longer than 10.48 ms requires
89 knowing the start times precisely. This would be straightforward if the 9.1 ms
90 period of the function generator was stable and known to a better precision
91 than the 0.05 ns precision of the stops, which unfortunately may not be the
92 case. To circumvent this, the signal from the start generator was split into a
93 direct signal which was sent to one channel of the TDC, and a delayed signal used
94 to start the TDC. The time of the next start relative to a given one is therefore
95 measured for each event, provided the delay is known precisely. The delay was
96 produced by a length of cable, and was measured as 61 ns in a dedicated run

¹It's a testament to computing progress that just as in 1993, when data sizes of 0.5 Mbytes were deemed nearly prohibitive in this field [8], the data volumes described here may be considered trivial in the future.

97 in which the direct signal and delayed signals were swapped: the former started
 98 the TDC, and the latter was sent to one of the stop channels. To facilitate
 99 data management, the LabView DAQ controlling the TDC breaks the data into
 100 files typically corresponding to some five minutes in length. Software written
 101 in Java was then used to reconstruct the streams in a given file. The software
 102 interrupts a stream any time memory errors are encountered. We have found
 103 that the following TDC acquisition parameters ensure errors are few: 100 starts
 104 per memory transfer and 360 memory transfers per file (i.e. streams of 327 s
 105 per file)

106 To test the efficiency of our reconstruction, we ran this setup for some 5 min-
 107 utes using a 110 Hz ($T = 9.1$ ms) frequency square start signal, and used as
 108 stops a square signal coming from another function generator with a frequency
 109 of roughly 73 Hz ($T' = 13.7$ ms), then studied the differences between recon-
 110 structed stop times. The direct times were also sent to one of the stop channels.
 111 Let T be the true start period, and $T < T' < 2T$ be the true stop period.
 112 The starts arrive at times $t_i = iT$, and the stops at times $t'_j = \varepsilon + jT'$, where
 113 $0 \leq \varepsilon < T$ represents the arbitrary phase shift between the signals. The TDC
 114 in fact measures δ_j , the arrival time of stop j after its preceding start; recon-
 115 struction assumes that times t_i are known. Given the periods used, each start
 116 is followed by one or zero stops. The phase shift ε is constant between gaps
 117 (starts with no stops). Reconstruction of stops not separated by gaps is done
 118 by $T' = \delta_{i+1} - \delta_i + T$; for those separated by a gap, $T' = \delta_{i+1} - \delta_i + 2T$. If a start
 119 was followed by a stop, and both are lost because of some memory problem, then
 120 reconstruction will incorrectly overestimate the next stop times and the period
 121 T' will be overestimated as $\delta_{i+2} - \delta_i + T = T' + \Delta T$, where $\Delta T \equiv T' - T$. If a
 122 gap was lost, then T' will be underestimated as $\delta_{i+2} - \delta_i + T = \Delta T$. If only a
 123 stop is missed, then the period will be overestimated as $2T'$.

124 Fig. 2 shows examples of reconstructed start and stop times, as well as the
 125 histogram of the difference between consecutive start times and stop times.
 126 The mean values of these histograms determine T and T' respectively. The
 127 histogram of stop time differences is free of entries at or below ΔT and at or
 128 above $T' + \Delta T$ implying no starts or stops are missed and that the stream has
 129 been properly reconstructed over this ≈ 5 mn interval. As a control, we have
 130 manually degraded the same data set, removing one start and its stop, removing
 131 a start that is not followed by a stop, and removing a stop. As expected, these
 132 respectively induce misreconstructed periods at $T' + \Delta T$, at ΔT , and at $2T'$.
 133 As an additional consistency check, we have calculated the number of expected
 134 stops based on the ratio of measured start to stop periods and the number
 135 of observed starts. This yields an expected number of stops of 26873.8, in
 136 excellent agreement with the measured number of stops, 26873. We note that
 137 the reconstructed stop periods distribution (average 12.18 μ s) is asymmetric
 138 with a few periods that are shorter than expected (of the 36000 events, the
 139 shortest is 12.06 μ s). The standard deviation of 2 μ s for a period of 12 ms, is
 140 small, but greater than the corresponding numbers for the start period (7 ns
 141 for 9.1 ms). We are unable to conclude if this is caused by our technique or
 142 instabilities in the function generator.

143 In practice, the consequences of these small imperfections are unobserved, in
 144 part because if events are reconstructed over 1 ms for instance, then only one in
 145 nine events will overlap consecutive starts. Once software has reconstructed the
 146 streams, a second routine identifies coincidences and outputs the data in our
 147 usual MPCC format, so that our standard MPCC analysis routines can be used.
 148 We have tested our analysis pipeline from the identification of coincidences and
 149 on by generating simulated streams of data discussed in Sections 3 and 4. An-
 150 other test we have carried out is the comparison of results from the TDC and
 151 from the standard digitizer-based MPCC method with a National Instruments
 152 PXI 5154 digitizer used previously [11]. These results, in terms of average pulse
 153 shape, were obtained with a $20 \times 10 \times 5 \text{ mm}^3$ ZnWO_4 crystal at 3.4 K and
 154 are shown in Figure 3. The sample was provided by the CRESST collabora-
 155 tion, and ZnWO_4 is being actively considered as a scintillator for dark matter
 156 searches [6, 12, 13]. The figure shows that the two methods yield very similar
 157 results except at short times of the order of a few tens of nanoseconds, where the
 158 TDC underestimates the number of photons compared to the digitizer. This is
 159 consistent with the TDC not being able to resolve stops closer than 15 ns apart,
 160 whereas the digitizer and the offline photon identification routines can resolve
 161 individual photons separated by as little as 5 ns [11]. Other differences between
 162 the digitizer and the TDC include the fact that with the former, it is possible
 163 to obtain the amplitude, or the integral, of each photon pulse, and it is possi-
 164 ble to reanalyze data offline changing the threshold for the photon, whereas
 165 the TDC allows reanalysis of the data offline using different coincidence and
 166 acquisition windows. All in all, the TDC is a viable alternative to a digitizer
 167 for the MPCC technique, except perhaps at short time constants. It should be
 168 noted however that at very short time constants, the MPCC method itself is
 169 not recommended [6].

170 3. Choice of the coincidence window

171 Once continuous streams of photons have been obtained from the TDC for
 172 both PMs, a software algorithm looks for coincidences between the two channels,
 173 and, when one is found, identifies the times of photons for a given acquisition
 174 window, as illustrated in Figure 4. Unlike the digitizer based approach, in
 175 which both coincidence window (T_{coinc}) and acquisition window (T_{acq}) are set
 176 once and for all, with the TDC, these parameters can be adjusted after data
 177 have been taken. This is convenient since the scintillation time constant of the
 178 sample being studied is not necessarily known in advance, yet both parameters
 179 are related to it. We also note that in the standard hardware coincidence setup,
 180 the time of the second of the two photons involved determines the coincidence,
 181 whereas by software, the start of the coincidence can be chosen as either of the
 182 two photons. In both the hardware and software coincidence techniques, data
 183 are also recorded over a pretrigger usually chosen to include the coincidence
 184 window.

We first consider the influence of the coincidence window on the shape of
 the spectra, with no cuts applied to the data. For a given coincidence window

T_{coinc} , and a scintillator emitting uncorrelated photons with an exponential time constant τ such that n are detected by one PM and m by the other, the coincidence probability is:

$$p_{coinc} = 1 - e^{-nmT_{coinc}/\tau} \quad (1)$$

185 This expression, derived in Appendix A and generalized there to multiple time
 186 constants (Eq. A.8), depends on the dimensionless number nmT_{coinc}/τ which
 187 is the product of the number of photons and the coincidence window over the
 188 time constant. For a luminous scintillator with a short time constant or a long
 189 coincidence window, this number, and therefore the coincidence, probability is
 190 high. Conversely, for few photons, or a slow scintillator, or a short coincidence
 191 window, the number and the coincidence probability is low. One consequence of
 192 this is that for a given scintillator, coincidence window, and photons detection
 193 efficiency, the coincidence efficiency is lower for the low energy part of the en-
 194 ergy spectrum since there are fewer photons. This can distort the shape of the
 195 spectrum, mainly in terms of amplitudes of various lines, but could also shift
 196 some lines to a small extent. This last effect would be relevant when studying
 197 the linearity of a scintillator or its quenching factor for various particles. Cor-
 198 recting the photon spectra, which show the histograms of the sum of photons on
 199 both channels (i.e. $n + m$), for coincidence efficiency can be attempted by two
 200 approaches. In the bin-by-bin approach, one assumes that $n = m = \frac{n+m}{2}$ and
 201 corrects the spectrum by dividing each bin by the function $1 - e^{-\left(\frac{n+m}{2}\right)^2 T_{coinc}/\tau}$.
 202 In the more precise event-by-event approach, as each event is binned into the
 203 histogram, it is weighted by the inverse of $1 - e^{-nmT_{coinc}/\tau}$. The difference be-
 204 tween the two methods is rather small in our case since the optical efficiencies
 205 of the PMTs are similar, with the exception of cases in which the number of
 206 photons is low and statistical fluctuations become important.

207 In Fig. 5, we compare the theoretical coincidence efficiencies obtained from
 208 Equation 1 with simulated data that have been processed by the analysis pipeline.
 209 A data stream was generated for 10^4 events coming from a scintillator of time
 210 constant $1 \mu s$. To avoid pileup, the full stream is assumed to last $10^8 \mu s$. The
 211 expected number of photons generated for each event is itself drawn from a
 212 distribution that is flat with a maximum of 100 photons per channel. For each
 213 event, and each channel, there are Poisson fluctuations around the expected
 214 number of photons. The full set of photons is sorted by arrival time and written
 215 to a stream file. These simulated data are then fed into the analysis pipeline
 216 with various coincidence windows logarithmically spaced from $10^{-4} \mu s$ to $10^2 \mu s$.
 217 The analysis uses identical acquisition windows of $9 \mu s$ ensuring that more than
 218 99.9% of photons should be counted. The $1 \mu s$ preceding the coincidence is
 219 used for pretrigger. Figure 5 shows that the flat spectra are suppressed for low
 220 numbers of photons and small coincidence windows, and that the effect is well
 221 reproduced by Equation 1.

222 We have carried out a similar analysis using real data obtained from the
 223 CRESST $ZnWO_4$ crystal at 3.4 K in Fig. 6. The sample was exposed to α
 224 and γ particles from an ^{241}Am source, and concurrently to γ particles from a

225 ^{137}Cs source. Data were analyzed using a fixed acquisition window of 1.8 ms,
 226 a pretrigger of 0.2 ms, and coincidence windows ranging from 0.01 μs to 10 μs .
 227 The top figure shows the rough, uncorrected spectra. The α peak, around
 228 300 photons summed on both channels, is the same in all cases, but the lower
 229 662 keV ^{137}Cs line around 180 photons already shows some distortion, and there
 230 is more than an order of magnitude difference in the spectra around 50 photons.
 231 The larger coincidence windows also show some structure around 18 photons
 232 which is absent from the shorter coincidence windows. The position of this
 233 structure is consistent with it being the 60 keV line from ^{241}Am . The middle
 234 figure shows the efficiencies for different coincidence windows, assuming the
 235 time constants and numbers of photons obtained for ZnWO_4 and γ particles in
 236 a double-coincidence setup triggered 511 keV photons from a ^{22}Na source [11].
 237 Curves assume different number of photons on both channels, parametrized by
 238 R , the ratio of photons on each channel. The bottom figure shows the spectra
 239 corrected for the efficiency curves. The corrected spectra are in good agreement
 240 with one another down to at least 50 photons; i.e. the correction works for
 241 coincidence efficiencies at least as low as 10%. The spectra are now compatible
 242 around the 60 keV line in terms of position and amplitude, though the line
 243 is not resolved for the shorter windows. The positions and amplitudes of the
 244 60 keV line match for the longer coincidence windows. This buttresses our
 245 earlier identification of this line [14]. The spectra from the shorter coincidence
 246 windows are compatible with the presence of the same line though it can not
 247 be resolved from the noise. This shows that data taken using the standard
 248 MPCC technique with a poor choice of hardware coincidence window can not
 249 necessarily be corrected perfectly at low number of photons. Conversely, the
 250 flexibility afforded by the streaming TDC to adjust the coincidence window
 251 after data have been taken assists in understanding the coincidence efficiency
 252 and helps to ascertain the low energy features of the spectra.

253 4. Choice of the acquisition window

254 The next parameter we study is the duration of the acquisition window (T_{acq})
 255 over which photons are recorded. In the MPCC technique, the average time of
 256 pulses, defined as the average arrival time of photons after the first one, is used
 257 to reject events suffering from pileup [6]. However, in certain conditions, the
 258 average time of the pulse may itself be biased by pileup. For photons distributed
 259 according to several exponential distributions, the mean arrival time of photons
 260 counted from the start of the pulse over a time T_{acq} is

$$\begin{aligned}
 \frac{\int_0^{T_{acq}} t \frac{dn}{dt} dt}{\int_0^{T_{acq}} \frac{dn}{dt} dt} &= \frac{\sum n_i \tau_i (1 - e^{-T_{acq}/\tau_i} (1 + T_{acq}/\tau_i))}{\sum n_i (1 - e^{-T_{acq}/\tau_i})} \\
 &\leq \frac{\sum n_i \tau_i}{\sum n_i} \quad (2)
 \end{aligned}$$

261 (Appendix B). For an infinite window, this yields $\frac{\sum n_i \tau_i}{\sum n_i}$, referred to here as the
 262 effective time constant. For a shorter window, the value will be underestimated.

263 For long values, pile-up will lead to an overestimation of this parameter.

Once the average arrival time is determined, cuts based on the time of the first photon and on the average time can be applied to the data to reject pileup in certain cases, and the light yield can be studied with histograms of the number of photons. Using the same notations as before, the number of photons actually counted during acquisition window T_{acq} if there is no pileup will be:

$$\int_0^{T_{acq}} \frac{dn}{dt} dt = \sum_i n_i \left(1 - e^{-T_{acq}/\tau_i}\right) \leq \sum n_i \quad (3)$$

For an infinite window, this number is $\sum n_i$. If the acquisition window is too short, then photons will be missed. Practically, 90% of the photons can be counted for $T_{acq}/\tau = 2.3$. Another effect can occur when the acquisition window is too short compared to the time constant of the scintillator (Figure 4c): after a first coincidence is detected at the start of an event, the acquisition window is too short to cover the length of the pulse, and a second coincidence can be detected right after the acquisition window on the remaining photons. This second acquisition window will only contain a fraction of the photons which can appear as artefacts in the spectrum of the number of photons. This effect can be repeated again and again, introducing spurious features in the spectra with the following, decreasing, number of photons:

$$\nu_j \equiv \int_{jT_{acq}}^{(j+1)T_{acq}} \frac{dn}{d\tau} dt = \sum_i n_i e^{-jT_{acq}/\tau_i} \left(1 - e^{-T_{acq}/\tau_i}\right) \quad (4)$$

264 For example, a single time constant of $\tau = 165 \mu s$ and an acquisition window
 265 of $T_{acq} = 200 \mu s$ result in $\nu_0/n = 0.70$, $\nu_1/n = 0.21$ and $\nu_2/n = 0.06$. We do
 266 not attempt to calculate the number of events for each ν_j , though this may be
 267 possible by a reasoning on the coincidence probability of the remaining photons
 268 along the lines of that in Appendix A.

269 Moreover, if the acquisition window is too long, then there is a risk that
 270 pileup will occur. For instance, if the acquisition window is long compared
 271 to the average time between events, the spectrum of number of photons will be
 272 biased (Figure 4d). If the acquisition window also happens to be larger than the
 273 scintillation time constant, several events will be fully contained in the window,
 274 and the true number of photons (essentially $\sum n_i$) will give rise to spurious
 275 artefacts at integer multiples $j \sum n_i$.

276 We have studied the effect of the acquisition window using simulated streams
 277 of data. In these simulations, a given number of events (typically 10^3) are
 278 assumed to arrive randomly according to a uniform distribution over a given
 279 amount of time, with an average time between events of ΔT . For each event, the
 280 expected number of photons on each channel is fixed. For each event, the actual
 281 number of photons is set to the expected number (no Poisson fluctuations). Once
 282 all the events have been drawn, they are sorted by time and written to a stream
 283 file that is fed into the analysis pipeline. Results coming from a simulation with
 284 a single time constant of $\tau = 165 \mu s$ and Dirac delta function spectra centered

285 on 144 photons per channel are shown in Figures 7 ($\Delta T = 2 \times 10^{11} \mu\text{s}$, i.e. no
 286 pileup) and 8 ($\Delta T = 2 \times 10^4 \mu\text{s}$, much pileup). The data are first analyzed with
 287 the following standard MPCC cuts [6]: cut on first photon arrival time, test
 288 statistic cut. Then, the time structure of the events can be studied by building
 289 a histogram of the arrival times of the photons for events with a well-defined
 290 number of photons.

291 In the case of data with no pileup (Fig. 7), the mean arrival time and the
 292 total number of photons behave as expected from Equations 2 and 3. For the
 293 total number of photons, the mode of the distribution is more robust than
 294 the mean, and at very short window times (Fig. 7b₁), the distribution itself
 295 displays the artefacts described in Eq. 4 that may complicate determination
 296 of the mode. The fitted position of the three visible peaks is broadly consistent
 297 with what is expected from Eq. 4: 202.9 ± 0.2 photons (compared to $288 \times 0.7 =$
 298 201.6), 57.6 ± 0.2 (compared to $288 \times 0.21 = 60.5$), and 13.4 ± 0.3 (compared
 299 to $288 \times 0.06 = 17.3$). In addition, the reconstructed pulse shapes show an
 300 excess of events in the first time bin (Fig. 7c₁). This is a consequence of the
 301 time of each photon in an event being calculated relative to the first photon,
 302 rather than to the true start time of the event which is unknown. For small
 303 acquisition windows, this causes the result of an exponential fit to the histogram
 304 to underestimate the true time constant (the fit also includes a flat background).
 305 For larger acquisition windows however, the first bin has less weight relative
 306 to the others, and the fitted time constant closely matches the input of the
 307 simulation. One experimental modification that circumvents this problem and
 308 allows more precise measurements of short scintillation times is to use a fast
 309 extra scintillator and a tagged source [11]. Overall, on this clean data set, the
 310 expected time constant is properly reconstructed and the cuts play only a small
 311 role.

312 In the case of data with significant pileup (Fig. 8), the histogram of the
 313 number of photons (Fig. 8b₁) displays artefacts at positions similar to those in
 314 the no-pileup case when the acquisition window is short. The mean arrival time
 315 starts to diverge from the model when the acquisition window becomes long
 316 enough for pileup to become significant. For large acquisition windows (e.g.
 317 $T_{acq} = 100 \text{ ms}$, Fig. 8b₃), the distribution of the number of photons exhibits
 318 spurious peaks at multiples of the true number, as the window is large enough
 319 to include several events ($T_{acq} \gg \Delta T$), and the time constant of the events
 320 is also much smaller than the acquisition window ($T_{acq} \gg \tau$). When this is
 321 accounted for and the proper peak selected, the total number of photons follows
 322 the model. After cuts, the proper pulse shape is reconstructed, except for the
 323 longest windows in which the prevalence of pileup leads to the cuts rejecting
 324 too many events for a fit on the pulse shape to be performed (Fig. 8c₃).

325 A similar analysis is next carried out on ZnWO₄, at two temperatures (295 K
 326 and 3.4 K) illustrated in Fig. 9 and 10. Unlike the simulation, the time constant
 327 of ZnWO₄ at various temperatures is not known *a priori*. The analysis has been
 328 carried out with a 900 ns coincidence window. As the crystal cools, the effective
 329 time constant increases by an order of magnitude from $\approx 10 \mu\text{s}$ to $\approx 200 \mu\text{s}$.
 330 This increase is broadly consistent with fluorescence measurements [15]. At both

331 temperatures, for short acquisition windows, the average time increases with the
332 acquisition window (Fig. 9a and 10a). There is then a plateau during which the
333 average time is independent of acquisition window. Up to here, there is good
334 agreement with Eq. 2. However, when the window becomes too long, pileup
335 appears and the average time increases once more, though the mode is slightly
336 more robust. From the standpoint of the number of photons, the short windows
337 contain an artefact echoing the main α line in the spectra, as per Eq. 4 (Fig. 9b₂
338 and 10b₂). In the long acquisition windows, there are also artefacts at integer
339 multiples of the α line (Fig. 9b₃ and 10b₃). As the acquisition window changes,
340 the position of the α line itself follows the model in Eq. 3 until pileup causes it
341 to be overestimated (Fig. 9b and 10b). The cuts allow the average pulse shape
342 to be reconstructed in a way that does not depend very much on the acquisition
343 window, except at low temperatures and short windows. Pulses have been
344 fitted using 2 exponentials and a constant at 295 K, and using 3 exponentials
345 and a constant at low temperature. Overall, since the time constants of the
346 crystal change with temperature, an acquisition window that is correct at room
347 temperature (e.g. 0.1 ms) may not be optimal at low temperature; and the
348 TDC allows to make up for this after data have been taken. This is important
349 in particular to understand whether features in a spectrum are real (i.e. the
350 60 keV line from ²⁴¹Am) or artefacts (echoes of the α line from ²⁴¹Am). We
351 defer the study of the differences in time constants between alpha and gamma
352 particles to future work.

353 5. Transmission of optical cryostat

354 We have also used the TDC to study the transmission of the optical cryo-
355 stat used in these measurements. The cryostat is closed-cycle, with the compact
356 optical design of a previous one [5]. The three sets of windows, at room tem-
357 perature, 70 K and 4 K (the last two values are nominal), are made out of
358 fused silica to obtain good transmission over a broad spectral range, and have a
359 nominal transmission of more than 90% between at least 200 nm and 1000 nm.
360 Temperature-induced variations in their transmission could affect the measured
361 light yields at various temperatures. Therefore, a setup has been built to mea-
362 sure the transmission at a given temperature, relative to the transmission at
363 room temperature. It is illustrated in Figure 11. On one side of the cryostat,
364 along its optical axis, is a LED, followed by an optical filter and a collima-
365 tor. Off-axis is a first, collimated, reference PM that serves to monitor the
366 stability of the LED. On the other side of the cryostat is an on-axis, collimated
367 photomultiplier that measures the light transmitted through the cryostat. The
368 collimators and intensity of the LED are chosen so that the PMs see individual
369 photons, at a rate of one to a few kHz. The PMs are Hamamatsu R7207, which
370 have a broad spectral response (greater than 10% quantum efficiency over the
371 150 nm–530 nm range), and a low rate of dark counts (nominally below 30 Hz).
372 At each temperature, photons are counted on both PMs with the TDC for a
373 given amount of time, and the ratio of counts is calculated after subtraction
374 of dark counts (the dark counts were measured in a dedicated run with the

375 LED off). This provides the relative evolution of the light yield as a function
376 of temperature, but not an absolute measurement of the transmission at each
377 temperature. Taking the ratio of the transmission and reference PMs cancels
378 out any instabilities in the LED. Two LEDs have in fact been used, one emitting
379 white light, and one emitting UV light. To check the stability of the system, a
380 measurement was taken with each LED and the apparatus on the cryostat at
381 room temperature. Over 2.5 day with the white LED, the ratio of PM counts
382 showed fluctuations with a standard deviation of 0.4% of the mean value. This
383 provides an estimate of systematic instabilities in the system, including effect of
384 precise room temperature on the LED and each PM, and other environmental
385 sources of noise on the PMs. Measurements have been made at four different
386 wavelengths, using optical filters centered at 280 nm (UV LED), 435 nm, 488 nm
387 and at 600 nm (white LED). At each wavelength, measurements were carried out
388 at three temperatures (289 K, 77 K and 4 K). Results are shown in Figure 12.
389 Reported errors come from propagating the statistical error on the number of
390 counts seen on each PM, and are one standard deviation. For the three lowest
391 wavelength measurements, the transmission varies by less than 0.5% relative to
392 room temperature. At the longest, orange, wavelength, the variation could be
393 as large as 1.5%. This result in particular may in fact be dominated by system-
394 atics mentioned earlier influencing the rates on each PM, since both PMs show
395 a roughly 10% increase in rate at low temperatures, but the increase is slightly
396 greater for the reference PM. Nonetheless, overall, these variations are small and
397 will have a limited effect on relative light yield measurements of scintillators.

398 6. Conclusion

399 In the context of a study of scintillators at low temperatures, we have oper-
400 ated a time-to-digital converter (TDC) in streaming mode to identify photons
401 later analyzed offline using the multiple photon counting coincidence technique
402 to extract timing and light yield information. Streams of duration 5 minutes
403 have been achieved. Compared to the standard approach that involves a hard-
404 ware trigger and a digitizer with a fixed acquisition window, being able to chose
405 the coincidence window and acquisition window offline provides greater flex-
406 ibility and facilitates understanding of spectral features from the scintillator,
407 as demonstrated here with the 60 keV line from ^{241}Am shining on a ZnWO_4
408 crystal. In addition, the amount of TDC data needing to be stored and pro-
409 cessed is significantly reduced compared to a digitizer. The main drawbacks of
410 the TDC-based method are the slightly greater deadtime between pulses, and
411 the lack of amplitude or integral information — though neither is generally an
412 issue for the long time constants encountered with many scintillators at low
413 temperatures. TDC models with less deadtime between pulses than the model
414 employed here and native ability to stream for hours exist. The TDC has also
415 been used to verify that the changes in optical transmission of the cryostat used
416 to cool the samples at various temperatures are small. The methods described
417 here can be directly extended to double coincidence measurements allowing im-

418 proved timing accuracy [11], and will be used to further the low-temperature
 419 study of scintillators under α and γ radiation.

420 7. Acknowledgements

421 We thank Federica Petricca and Franz Pröbst of MPP Munich for providing
 422 the ZnWO_4 sample. Sylvie Chapuy from Agilent Technologies kindly com-
 423 mented on the U1051A section of this manuscript. Summer students Con-
 424 nor Behan, Maïca Clavel and Florian Duquerroix made early contributions
 425 respectively to the TDC DAQ, the stream reconstruction software, and the
 426 coincidence efficiency studies and transmission measurements. This work is
 427 supported by NSERC Canada (Grant SAPIN No. 386432) and CFI-LOF and
 428 ORF-SIF (Project No. 24536). G. O. was supported by the Dutch Stichting
 429 voor Fundamenteel Onderzoek der Materie (FOM) under Programme 114.

430 Appendix A. Derivation of coincidence efficiencies

431 Given n photons arriving on one channel according to an exponential distri-
 432 bution $1/\tau e^{-t/\tau}$, and m photons on the other according to the same distribu-
 433 tion (both distributions have the same start time), for a window of given length
 434 T_{coinc} , what is the probability that it contains at least one photon from each
 435 channel (i.e. a coincidence)?

First consider the case of two photons arriving independently at times t_1
 and t_2 , one on each channel. The joint probability density function is:

$$\frac{d^2\mathcal{P}}{dt_1 dt_2} \equiv \frac{1}{\tau^2} e^{-(t_1+t_2)/\tau} H(t_1)H(t_2), \quad (\text{A.1})$$

436 where H is the Heaviside step function with a value of 0 for strictly negative
 437 arguments and a value of 1 for positive or null arguments. Assume that $t_1 < t_2$.
 438 Then the probability that the second photon is not coincident, i.e. that it arrives
 439 after time $t_1 + T_{coinc}$, is

$$\begin{aligned} \mathcal{P}(t_2 > t_1 + T_{coinc}) &= \int_0^{+\infty} \int_{t_1+T_{coinc}}^{+\infty} \frac{d^2\mathcal{P}}{dt_1 dt_2} dt_1 dt_2 \\ &= \frac{1}{2} e^{-T_{coinc}/\tau}. \end{aligned} \quad (\text{A.2})$$

440 The same value is obtained assuming that the other photon arrives first ($t_2 < t_1$):
 441 $\mathcal{P}(t_1 > t_2 + T_{coinc}) = \frac{1}{2} e^{-T_{coinc}/\tau}$. The overall probability of non-coincidence
 442 between these two photons is therefore the first probability or the second one,
 443 i.e. the sum:

$$\begin{aligned} p &\equiv \mathcal{P}(|t_2 - t_1| > T_{coinc}) = 2\mathcal{P}(t_2 > t_1 + T_{coinc}) \\ &= e^{-T_{coinc}/\tau}. \end{aligned} \quad (\text{A.3})$$

444 Now assume that one photon arrives on one channel at t_1 and n photons
 445 arrive on the other at t'_1, t'_2, \dots, t'_n . Assuming all of these events are independent,
 446 then there is non-coincidence overall if the t_1 is not coincident with t'_1 and t_1
 447 is not-coincident with t'_2 and so forth. In other words, the probability of non-
 448 coincidence is the product of the individual probabilities of non-coincidence:
 449 $p_{1n} \equiv p^n = e^{-nT_{coinc}/\tau}$.

We lastly consider the case where n photons arrive on the first channel, and
 m on the second, all independently. There is non-coincidence overall if the first
 photon on the first channel is coincident with no photons on the second channel
 (p_{1m}), and the second photon on the first channel is coincident with no photons
 on the second channel (p_{1m} again), and so forth for all the photons on the first
 channel. The overall probability of non-coincidence is therefore $p_{nm} \equiv p_{1m}^n =$
 $e^{-nmT_{coinc}/\tau}$. The probability that there is a at least one coincidence between
 the two channels is therefore:

$$p_{\text{coinc}} = 1 - p_{nm} = 1 - e^{-nmT_{coinc}/\tau} \quad (\text{A.4})$$

450 where τ is the time constant on both channels, T_{coinc} is the coincidence window,
 451 and n and m are the number of photons on each channel.

Generalizing this expression to pulse shapes with multiple time constants is
 straightforward. For instance, for a probability density function $\sum_{i=1}^N \frac{f_i}{\tau_i} e^{-t/\tau_i}$
 (where $\sum_{i=1}^N f_i = 1$), the joint probability density function becomes:

$$\frac{d^2\mathcal{P}}{dt_1 dt_2} \equiv \sum_{i=1}^N \frac{f_i}{\tau_i} e^{-t_1/\tau_i} \sum_{j=1}^N \frac{f_j}{\tau_j} e^{-t_2/\tau_j} H(t_1)H(t_2), \quad (\text{A.5})$$

452 then, if $t_1 < t_2$, the probability that there is no coincidence is:

$$\begin{aligned} \mathcal{P}(t_2 > t_1 + T_{coinc}) &= \int_0^{+\infty} \int_{t_1 + T_{coinc}}^{+\infty} \frac{d^2\mathcal{P}}{dt_1 dt_2} dt_1 dt_2 \\ &= \sum_{i=1}^N \sum_{j=1}^N \frac{f_i}{\tau_i} \frac{f_j}{\tau_j} \int_0^{+\infty} e^{-t_1/\tau_i} \\ &\quad \int_{t_1 + T_{coinc}}^{+\infty} e^{-t_2/\tau_j} dt_2 dt_1 \\ &= \sum_{i=1}^N \sum_{j=1}^N f_i f_j \frac{\tau_j}{\tau_i + \tau_j} e^{-T_{coinc}/\tau_j}. \end{aligned} \quad (\text{A.6})$$

453 The probability of non-coincidence between two photons, one on each channel,
 454 is twice this amount:

$$\begin{aligned} p &\equiv \mathcal{P}(|t_2 - t_1| > T_{coinc}) \\ &= 2\mathcal{P}(t_2 > t_1 + T_{coinc}) \\ &= 2 \sum_{i=1}^N \sum_{j=1}^N f_i f_j \frac{\tau_j}{\tau_i + \tau_j} e^{-T_{coinc}/\tau_j}. \end{aligned} \quad (\text{A.7})$$

By the same reasoning as previously, it follows that the probability of coincidence between n and m photons on each channel is:

$$p_{\text{coinc}} = 1 - \left(2 \sum_{i=1}^N \sum_{j=1}^N f_i f_j \frac{\tau_j}{\tau_i + \tau_j} e^{-T_{\text{coinc}}/\tau_j} \right)^{nm} \quad (\text{A.8})$$

455 Appendix B. Average time and number of photons

We first consider a scintillator emitting photons with a single time constant τ . The system detects n of these photons. The time distribution of these photons will be:

$$\frac{dn}{dt} = H(t) \frac{n}{\tau} e^{-t/\tau}. \quad (\text{B.1})$$

where H is the Heaviside step function. If $T_{\text{acq}} \geq 0$ is the acquisition window starting at $t = 0$, then the number of photons actually counted will be

$$\int_0^{T_{\text{acq}}} \frac{dn}{dt} dt = n \left(1 - e^{-T_{\text{acq}}/\tau} \right) \leq n. \quad (\text{B.2})$$

456 For an infinite window, this number is n . If the acquisition window is too short,
457 then photons will be missed. In practice 90% should be counted for $T_{\text{acq}}/\tau = 2.3$.

458 The mean arrival time of photons is given by:

$$\begin{aligned} \frac{\int_0^{T_{\text{acq}}} t \frac{dn}{dt} dt}{\int_0^{T_{\text{acq}}} \frac{dn}{dt} dt} &= \frac{n \left(-T_{\text{acq}} e^{-T_{\text{acq}}/\tau} + \tau \left(1 - e^{-T_{\text{acq}}/\tau} \right) \right)}{n \left(1 - e^{-T_{\text{acq}}/\tau} \right)} \\ &= \tau \frac{1 - e^{-T_{\text{acq}}/\tau} \left(1 + T_{\text{acq}}/\tau \right)}{1 - e^{-T_{\text{acq}}/\tau}} \\ &\leq \tau. \end{aligned} \quad (\text{B.3})$$

459 For an infinite window, this yields τ . For a shorter window, the value will be
460 underestimated.

In the more general case of a scintillator emitting with several time constants, the time distribution of these photons will be:

$$\frac{dn}{dt} = H(t) \sum_i \frac{n_i}{\tau_i} e^{-t/\tau_i}. \quad (\text{B.4})$$

The number of photons integrated over time T_{acq} will be:

$$\int_0^{T_{\text{acq}}} \frac{dn}{dt} dt = \sum_i n_i \left(1 - e^{-T_{\text{acq}}/\tau_i} \right) \leq \sum_i n_i \quad (\text{B.5})$$

461 The mean arrival time of photons is given by:

$$\begin{aligned}
\frac{\int_0^{T_{acq}} t \frac{dn}{dt} dt}{\int_0^{T_{acq}} \frac{dn}{dt} dt} &= \frac{\sum n_i (-T_{acq} e^{-T_{acq}/\tau_i} + \tau_i (1 - e^{-T_{acq}/\tau_i}))}{\sum n_i (1 - e^{-T_{acq}/\tau_i})} \\
&= \frac{\sum n_i \tau_i (1 - e^{-T_{acq}/\tau_i} (1 + T_{acq}/\tau_i))}{\sum n_i (1 - e^{-T_{acq}/\tau_i})} \quad (\text{B.6}) \\
&\leq \frac{\sum n_i \tau_i}{\sum n_i}
\end{aligned}$$

462 References

- 463 [1] P. C. F. Di Stefano, F. Petricca (Eds), Papers from the Fourth Workshop
464 on Cryogenic Scintillation CryoScint08, *Opt. Mat.* 31 (2009) 1381–1427.
- 465 [2] V. B. Mikhailik, H. Kraus, *Phys. Stat. Sol. (b)* 247 (2010) 1583–1599.
- 466 [3] R. F. Lang, W. Seidel, *New J. Phys.* 11 (2009) 105017.
- 467 [4] P. A. Rodnyi, *Physical Processes in Inorganic Scintillators*, CRC-Press, 1
468 edition, 1997.
- 469 [5] M.-A. Verdier, P. C. F. Di Stefano, F. Bonte, B. Bret, M. De Jesus,
470 G. Marot, T. Trollier, S. Vanzetto, *Rev. Sci. Instr.* 80 (2009) 046105–3.
- 471 [6] H. Kraus, V. Mikhailik, D. Wahl, *Nucl. Instrum. Methods A* 553 (2005)
472 522–534.
- 473 [7] L. M. Bollinger, G. E. Thomas, *Rev. Sci. Instr.* 32 (1961) 1044–1050.
- 474 [8] W. Moses, *Nucl. Instrum. Methods A* 336 (1993) 253–261.
- 475 [9] User manual, Agilent Acqiris time to digital converters (U1092-90017),
476 2010.
- 477 [10] J. Meister, U1051A TDC module absolute time recovery (Agilent Tech-
478 nologies, unpublished), 2010.
- 479 [11] M.-A. Verdier, P. C. F. Di Stefano, P. Nadeau, C. Behan, M. Clavel, C. Du-
480 jardin, *Phys. Rev. B* 84 (2011) 214306.
- 481 [12] I. Bavykina, G. Angloher, D. Hauff, M. Kiefer, F. Petricca, F. Pröbst, *Opt.*
482 *Mat.* 31 (2009) 1382–1387.
- 483 [13] H. Kraus, F. Danevich, S. Henry, V. Kobychyev, V. Mikhailik, V. Mokina,
484 S. Nagorny, O. Polischuk, V. Tretyak, *Nucl. Instrum. Methods A* 600 (2009)
485 594–598.
- 486 [14] M.-A. Verdier, P. C. F. Di Stefano, E. Mony, P. Nadeau, W. Rau, *IEEE*
487 *Trans. Nucl. Sci.* accepted (2012).

- 488 [15] V. Babin, P. Bohacek, E. Bender, A. Krasnikov, E. Mihokova, M. Nikl,
489 N. Senguttuvan, A. Stolovits, Y. Usuki, S. Zazubovich, Rad. Meas. 38
490 (2004) 533–537.

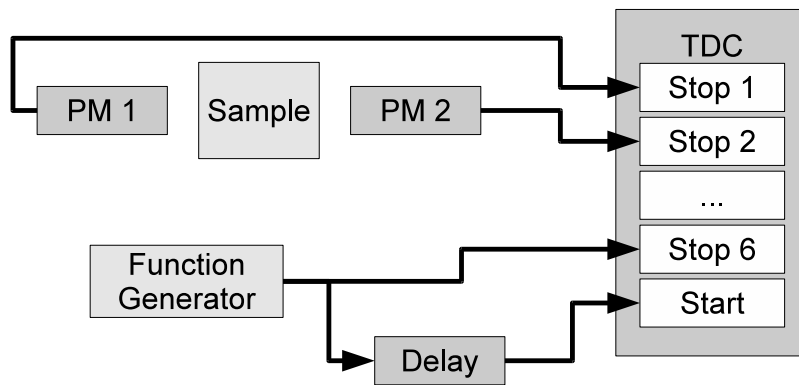


Figure 1: Setup used to obtain streams of data from the TDC as applied to the MPCC technique. A delayed signal from a periodic function generator starts the TDC. The direct signal from the function generator, as well as the two signals from the PMs, are fed into the stop channels of the TDC. To precisely measure the delay (created by a long wire), the direct and delayed lines from the function generator are swapped in a dedicated measurement. The optical cryostat has been omitted for clarity.

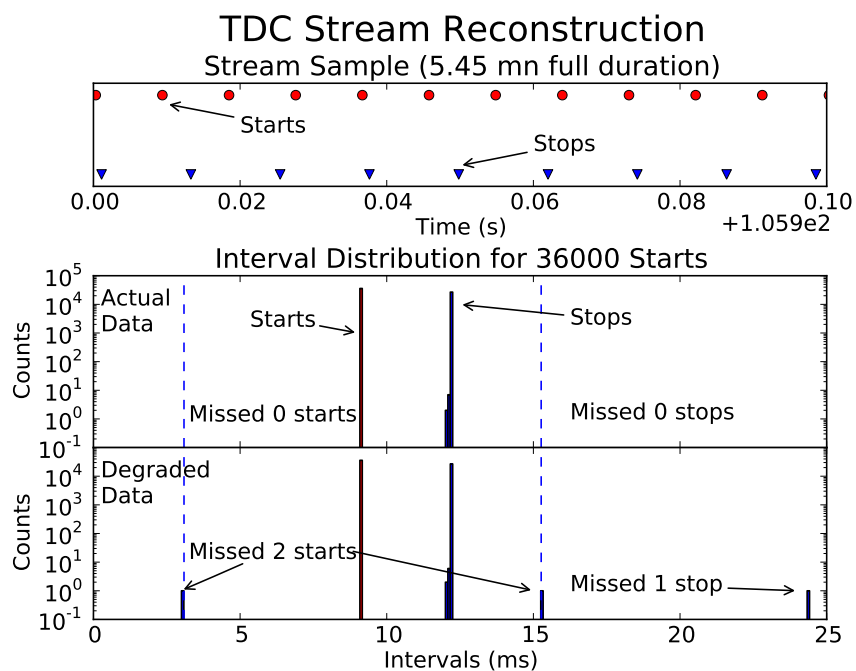


Figure 2: Top: reconstructed pattern of TDC 36000 starts and stops. Full stream lasts roughly 5 mn. Starts and stops have different periods. Middle: intervals calculated from above streams. No events are observed outside of the dashed blue lines, indicating no starts or stops have been missed during reconstruction. Bottom: same as middle, but with data that have been voluntarily degraded to evidence two types of missed starts and one type of missed stop.

ADC vs. TDC, ZnWO₄, ²⁴¹Am, 3.4 K

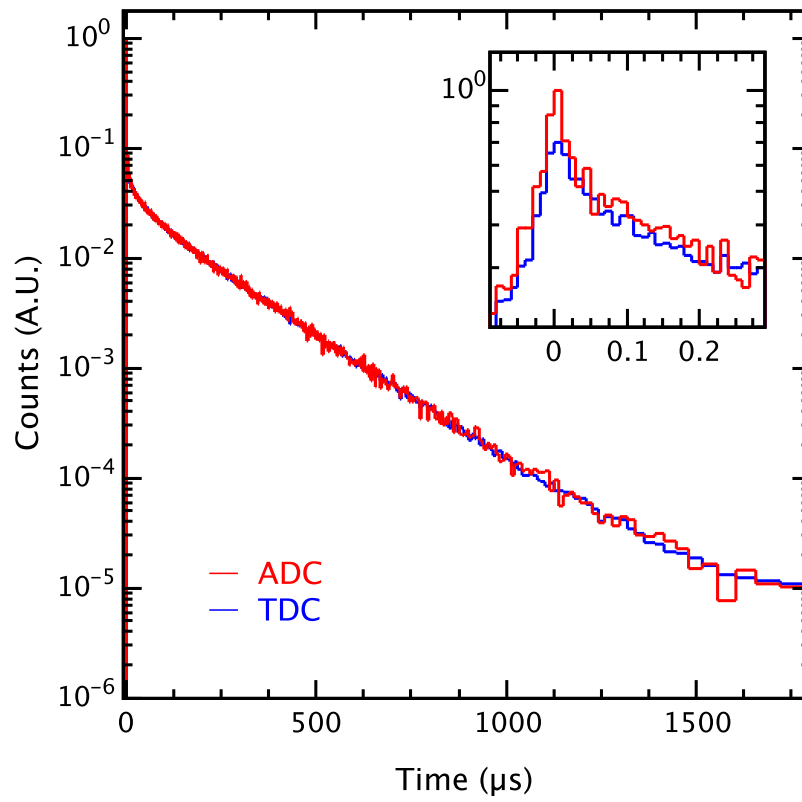


Figure 3: Comparison of pulse shapes obtained with the MPCC method using either the TDC or a digitizer (ADC). Pulses have been normalized so that the main decays overlap. The shapes are identical except for the shortest times, since the deadtime between TDC stops is greater than that obtained with the digitizer.

Coincidence Detection in Gedanken Stream

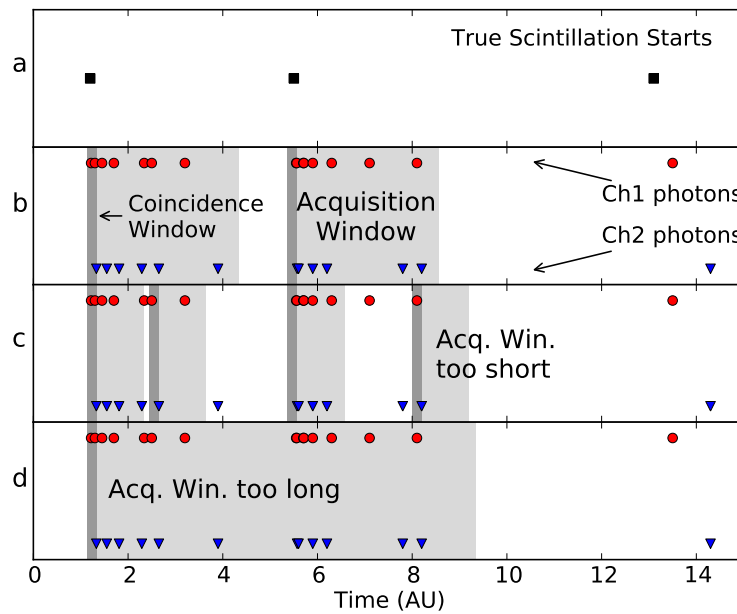


Figure 4: Sketch of detection of events in reconstructed stream. a) Actual start of random scintillation events, not directly measured. b) Arrival time of photons on both channels, and illustration of coincidence windows (dark gray) and acquisition windows (light gray). c) Example of an acquisition window that is too short, leading to multiple coincidence and triggers on a same scintillation event. d) Example of an acquisition window that is too long, leading to overestimation of photons in a given event. Pretrigger region has been omitted for clarity.

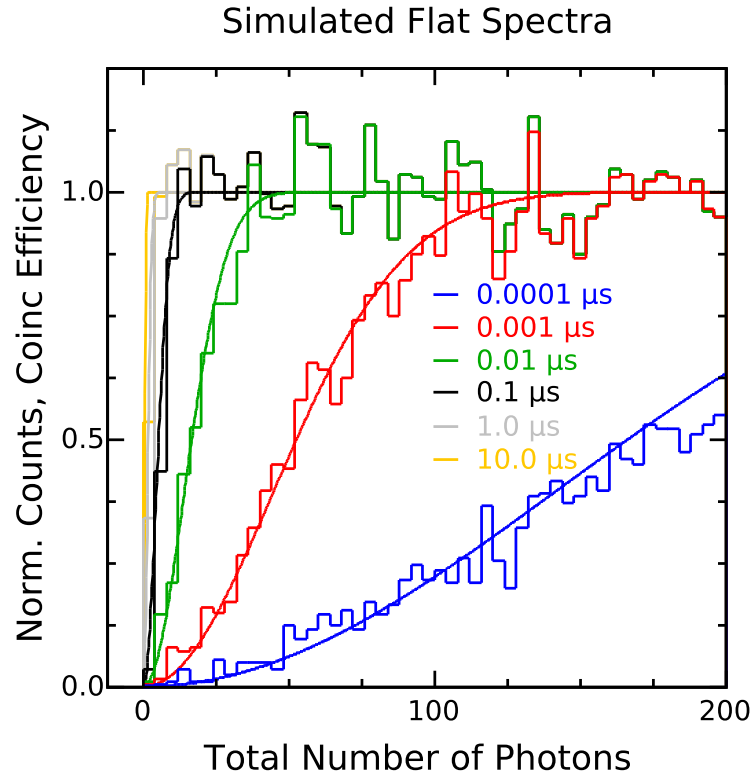


Figure 5: Comparison of calculated coincidence efficiencies and a simulated flat spectrum processed by the analysis pipeline, for various coincidence windows. Time constant of the scintillator used in simulation is $1 \mu\text{s}$; for each event, the number of photons on each channel are drawn from a Poisson distribution whose expected value is itself drawn from a uniform distribution with maximum 100. Abscissae in the plot are the sum of photons on both channels. Spectra are normalized to number of events in the simulation. For a given coincidence window, as the number of photons increases, so does the probability of coincidence. For a given number of photons, as the coincidence window increases, so does the probability of coincidence. The effect is well represented by Eq. 1. For clarity in this figure and the next, error bars are omitted but can be estimated from the bin-to-bin fluctuations.

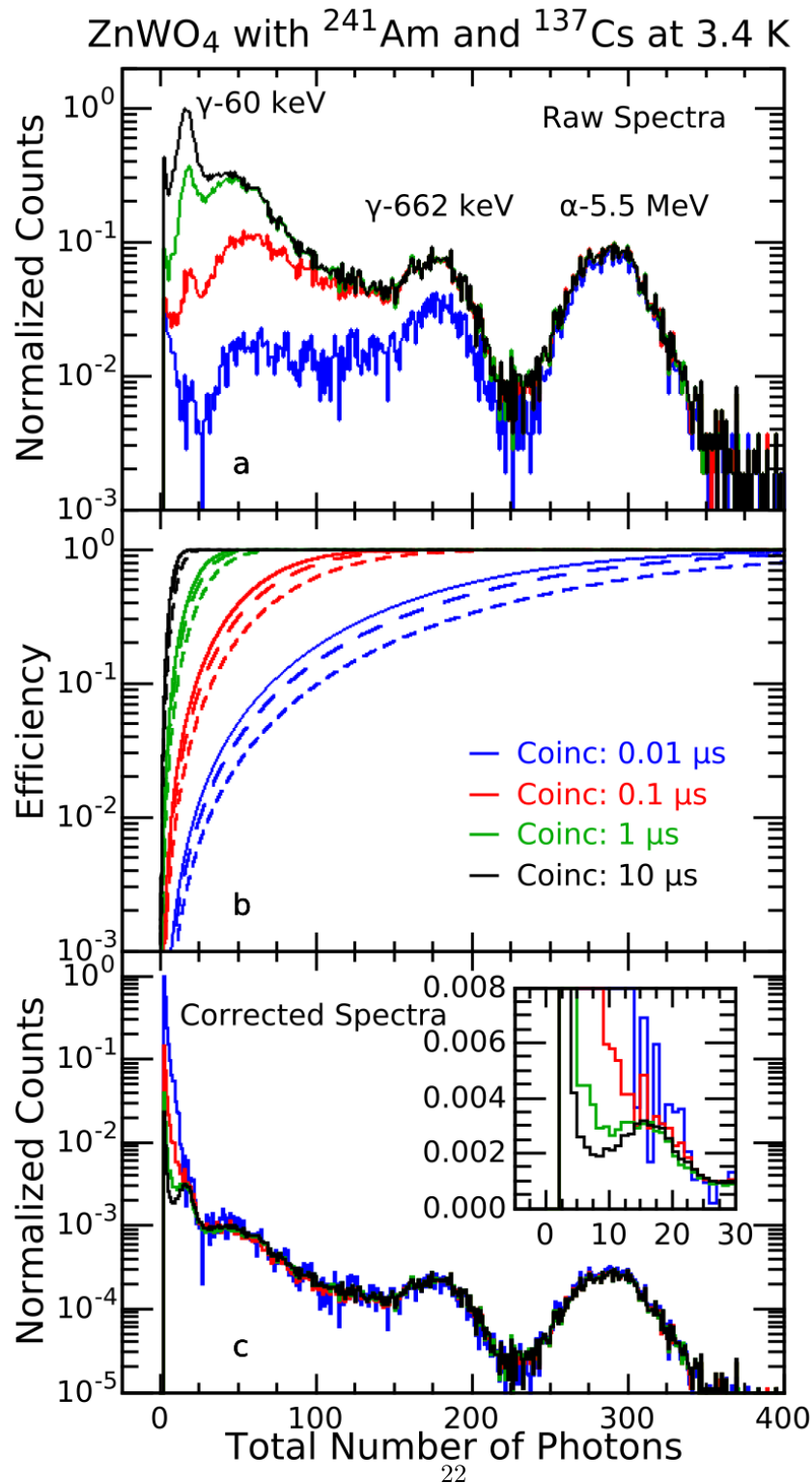


Figure 6: Effect of coincidence window length on spectra obtained from a ZnWO₄ crystal exposed to α particles from a ²⁴¹Am source and to γ particles from a ¹³⁷Cs source, at a temperature of 3.4 K. Top: raw spectra, for various coincidence windows. Middle: threshold efficiency functions derived from Eq. A.8. Calling R the ratio of photons in each channel, the solid curves are for $R = 1$, the long dashed ones for $R = 3$, and the short dashed ones for $R = 6$. Bottom: spectra corrected for threshold efficiency using the event-by-event method. Despite the correction, the low energy portion of the spectrum is not properly resolved if the coincidence window was too short (see insert with linear ordinates).

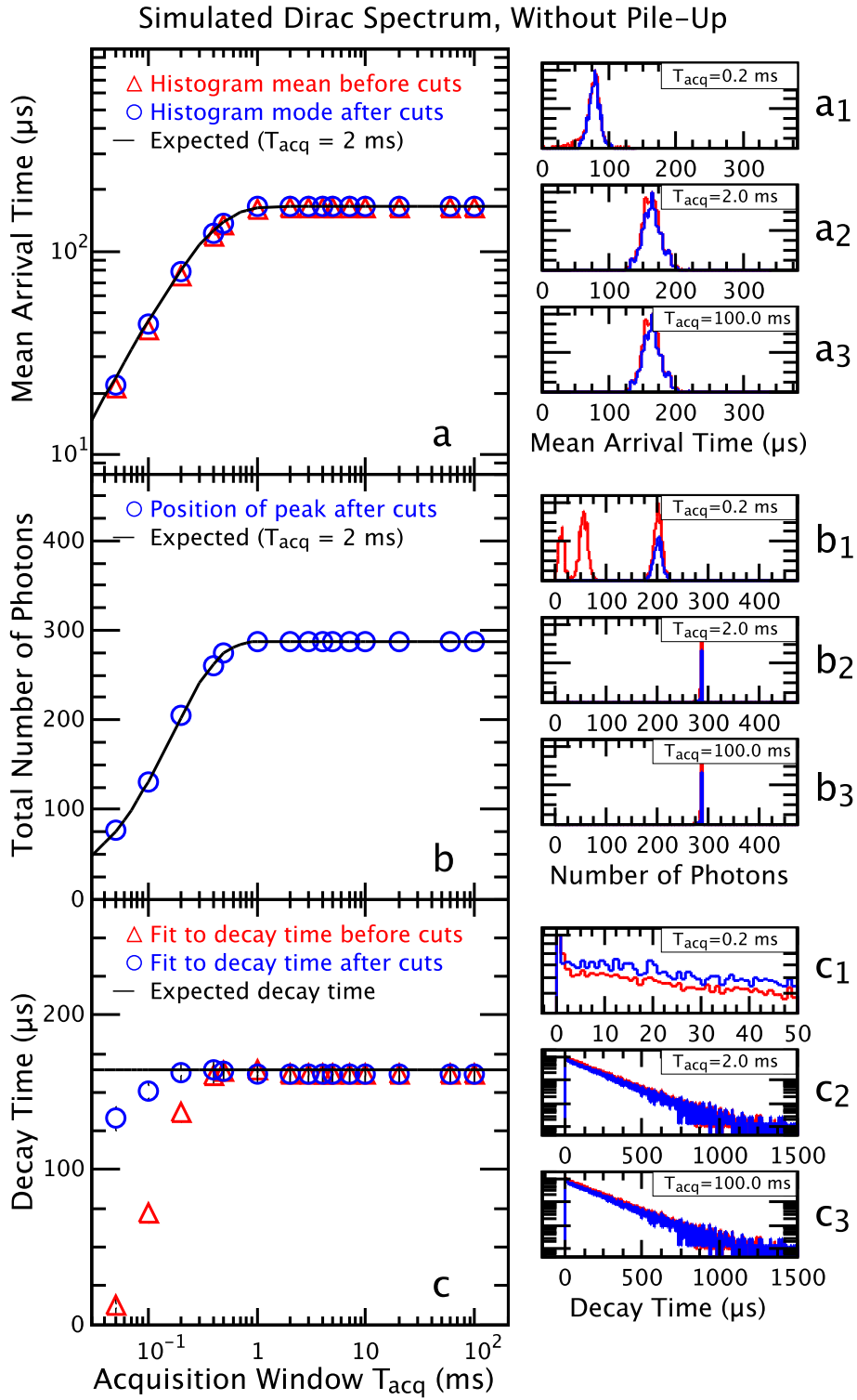


Figure 7: Results from 1000 simulated events drawn over $2 \times 10^{14} \mu\text{s}$ with 144 photons per event per channel and a single time constant of $165 \mu\text{s}$. Top: mean arrival time. Middle: total number of photons. Bottom: time constant determined from fit of average pulse. In all plots, green is before cuts, blue after. One standard deviation error bars are shown, but are often smaller than marker size. See text for discussion.

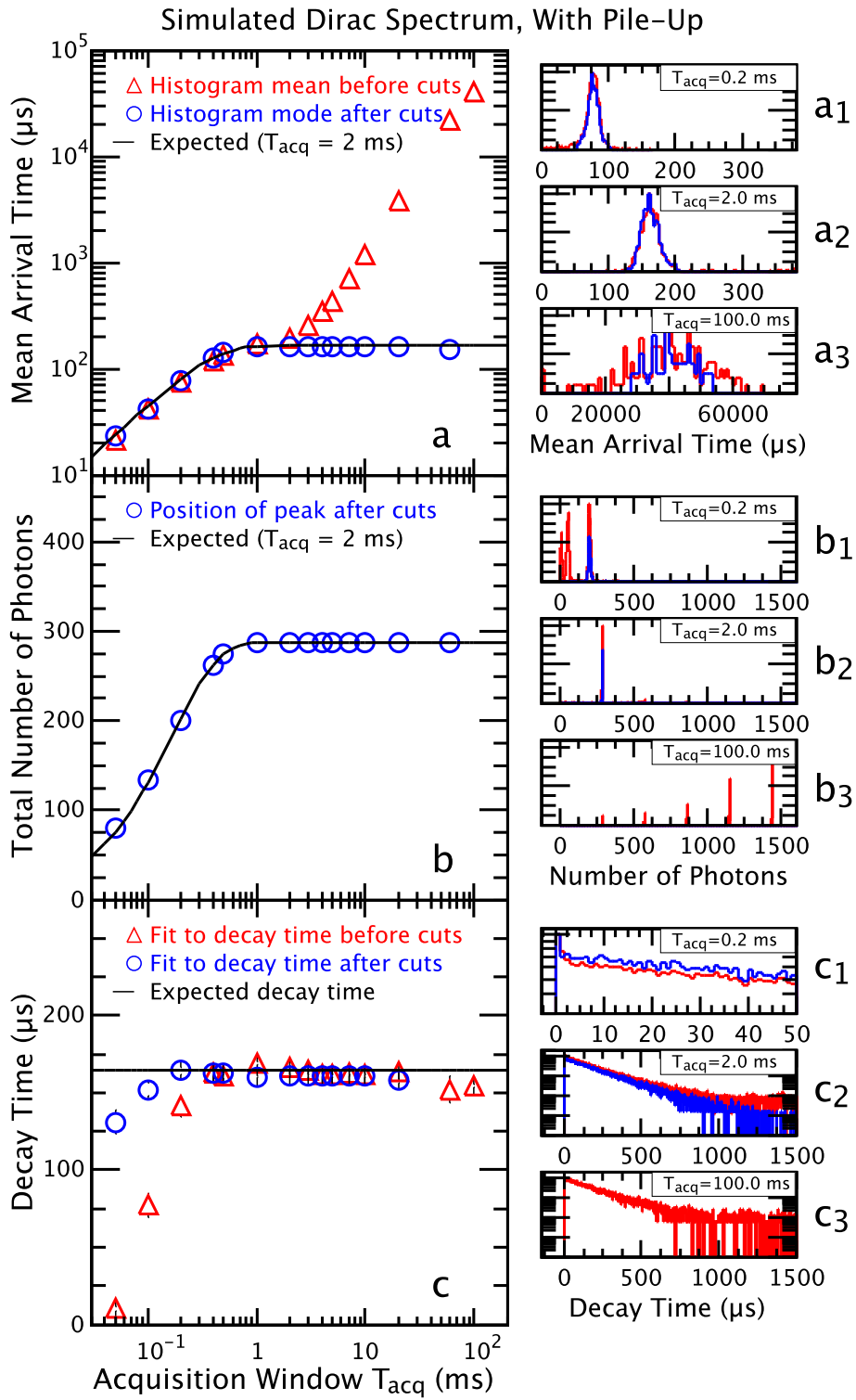


Figure 8: Simulation with same parameters as Fig. 7, but average time between events reduced to $2 \times 10^4 \mu\text{s}$ to simulate pileup.

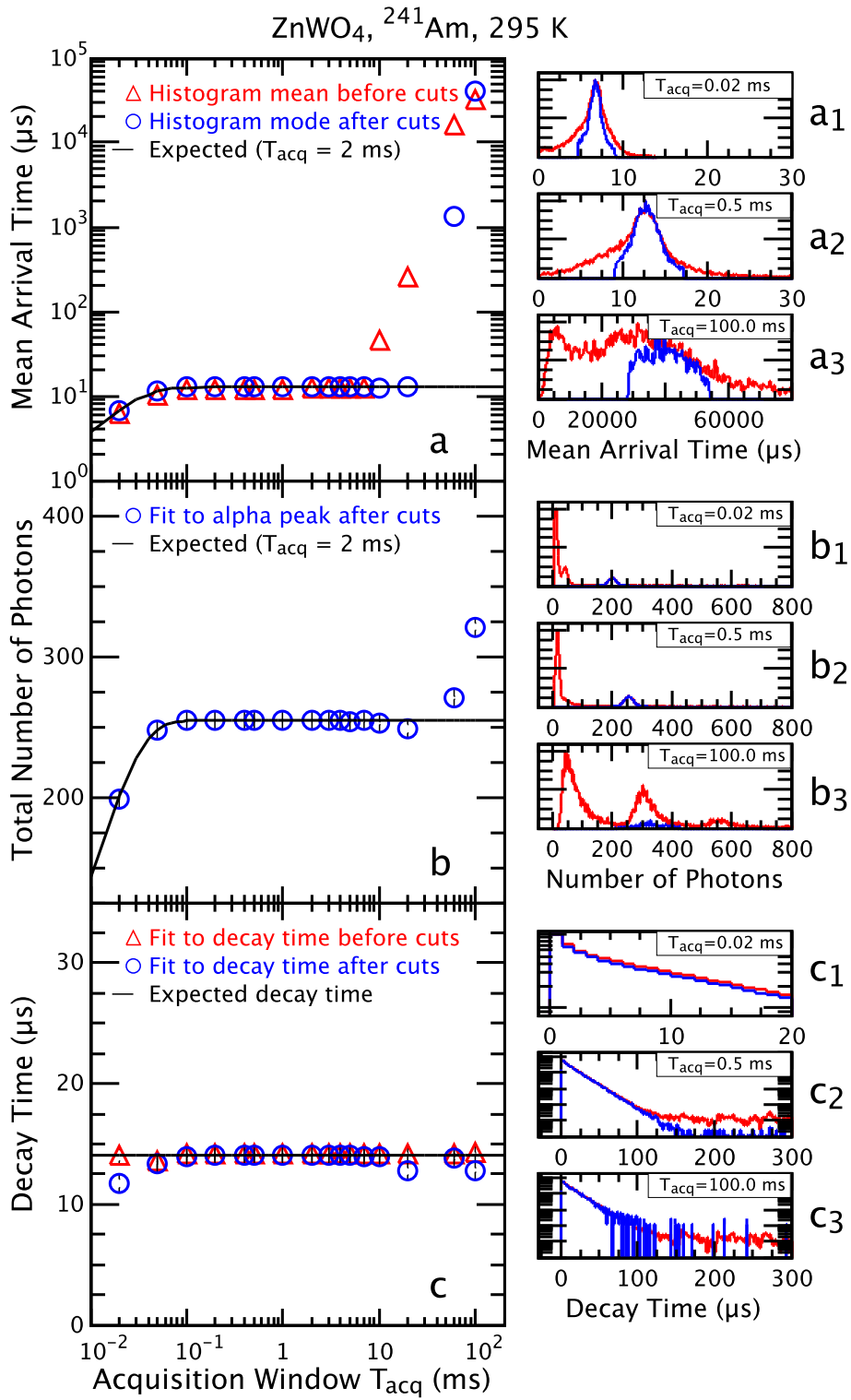


Figure 9: Same analysis as Fig. 7, but carried out on data from a ZnWO_4 crystal at 295 K exposed to a ^{241}Am source. Fits to pulse shape use 2 exponentials and a constant — only time constant with most photons is shown. See text for details.

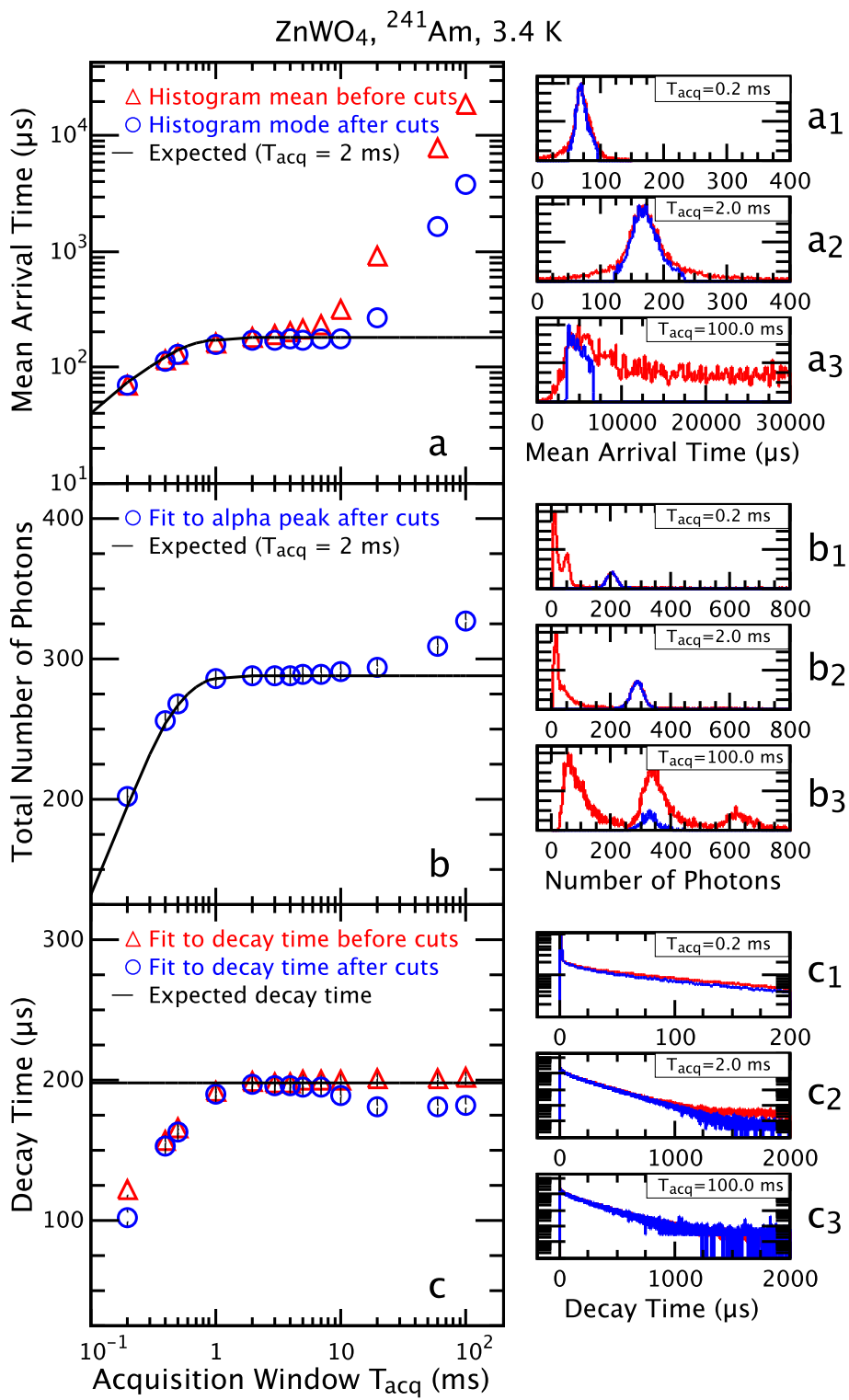


Figure 10: Same as Fig. 9, but ZnWO_4 crystal is now at 3.4 K, lengthening the time constants and increasing the light yield. Fits to pulse shape use 3 exponentials and a constant — only time constant with most photons is shown. See text for details.

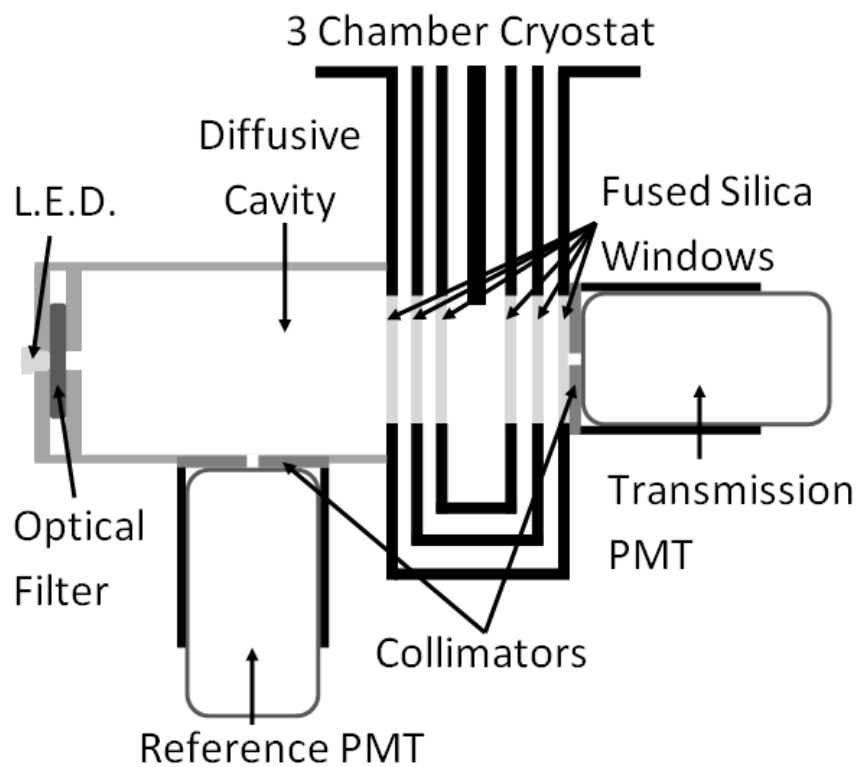


Figure 11: Setup to measure the optical transmission of the cryostat (not to scale). At each temperature, a LED, whose wavelength is selected by an optical filter, shines through the cryostat to the transmission PM. A reference PM, fore of the cryostat, monitors the stability of the LED.

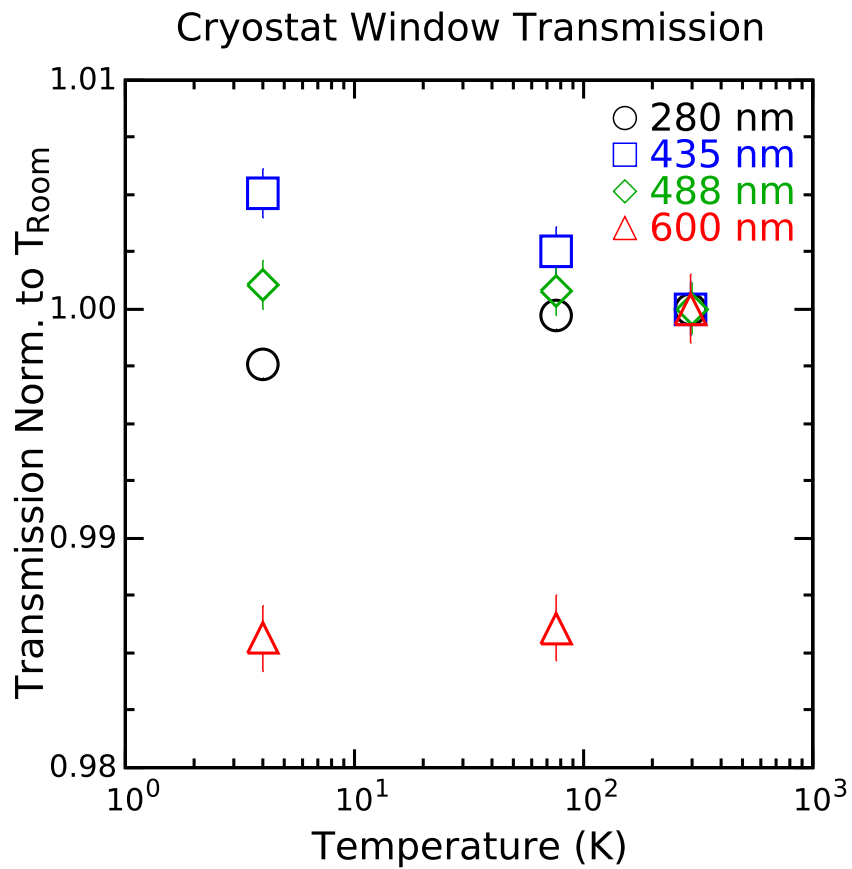


Figure 12: Optical transmission of the cryostat at various temperatures relative to room temperature, for different wavelengths. At the three shortest wavelengths, transmission varies by less than 0.5% over the temperature range; at the highest wavelength, variation is roughly 1.5%. Error bars are one standard deviation statistical ones. At the highest wavelength, systematic effects may dominate the results.